

RESEARCH ARTICLE

10.1002/2014JC010561

Key Points:

- Automated identification of breaking wave crests in thermal infrared imagery
- Remote estimates of wave energy dissipation rate in the surf zone
- Validation of the *Duncan* [1981] wave energy dissipation model in the field

Correspondence to:

R. J. Carini,
rjcarini@apl.washington.edu

Citation:

Carini, R. J., C. C. Chickadel, A. T. Jessup, and J. Thomson (2015), Estimating wave energy dissipation in the surf zone using thermal infrared imagery, *J. Geophys. Res. Oceans*, 120, doi:10.1002/2014JC010561.

Received 3 NOV 2014

Accepted 7 MAY 2015

Accepted article online 12 MAY 2015

Estimating wave energy dissipation in the surf zone using thermal infrared imagery

Roxanne J. Carini¹, C. Chris Chickadel¹, Andrew T. Jessup¹, and Jim Thomson¹¹Applied Physics Laboratory, University of Washington, Seattle, Washington, USA

Abstract Thermal infrared (IR) imagery is used to quantify the high spatial and temporal variability of dissipation due to wave breaking in the surf zone. The foam produced in an actively breaking crest, or wave roller, has a distinct signature in IR imagery. A retrieval algorithm is developed to detect breaking waves and extract wave roller length using measurements taken during the Surf Zone Optics 2010 experiment at Duck, NC. The remotely derived roller length and an in situ estimate of wave slope are used to estimate dissipation due to wave breaking by means of the wave-resolving model by Duncan (1981). The wave energy dissipation rate estimates show a pattern of increased breaking during low tide over a sand bar, consistent with in situ turbulent kinetic energy dissipation rate estimates from fixed and drifting instruments over the bar. When integrated over the surf zone width, these dissipation rate estimates account for 40–69% of the incoming wave energy flux. The Duncan (1981) estimates agree with those from a dissipation parameterization by Janssen and Battjes (2007), a wave energy dissipation model commonly applied within nearshore circulation models.

1. Introduction

Wave breaking is the primary forcing mechanism in the surf zone. Detailed spatial and temporal estimation of energy dissipation due to wave breaking is critical for improving models of nearshore processes, including circulation [Reniers and Battjes, 1997], wave-current interactions [Dally and Brown, 1995; Ruessink et al., 2001], and sediment transport [Plant et al., 1999; Lanckriet and Puleo, 2013]. However, measuring and modeling wave breaking in the surf zone is difficult due to bathymetry, currents, and the compounding influence of tides and weather. In situ estimation of wave energy dissipation typically requires an array of instruments that measure wave height and period [Thornton and Guza, 1986; Elgar et al., 1994; Madsen et al., 1997; Ruessink et al., 2001; Feddersen, 2012], from which the wave energy dissipation is computed as the wave energy flux gradient between instrument positions. This bulk dissipation is useful in calculating an energy balance over the entire surf zone, but breaking waves are episodic events with high spatial and temporal variability that cannot be fully captured by a necessarily sparse in situ instrument array. In contrast, remote sensing can provide unique spatial and temporal coverage for the process of wave breaking in the surf zone.

Applications of remote sensing to investigate dissipation due to wave breaking include visible, infrared, and microwave techniques (e.g., Romero et al. [2012], Jessup et al. [1997a, 1997b], and Catalán et al. [2011], respectively). In the evolution of a breaking wave, active foam refers to the foam generated at the crest while it is breaking and residual foam refers to the foam left in the wake after the breaking wave has passed. In visible imagery, active foam and residual foam both appear bright due to the diffuse reflection of light off bubbles that make up foam. Thus, it is difficult to use visible imagery to distinguish a wave roller from residual foam [Holman et al., 1993; Aarninkhof and Ruessink, 2004]. In thermal IR imagery, foam has a higher emissivity than foam-free water, making foam appear warmer than undisturbed water of the same temperature [Niclos et al., 2007]. The effect is especially pronounced near-grazing angles where the emissivity varies rapidly, resulting in a large contrast. Recent observations show that foam also appears to cool rapidly after it is formed and breaking subsides [Fogelberg, 2003; Marmorino and Smith, 2005]. This phenomenon suggests that IR imagery may be used to distinguish active foam from residual foam. The significant difference in the signature of active and residual foam in visible versus IR imagery is illustrated by the simultaneous visible and IR images of breaking waves in the surf zone in Figure 1.

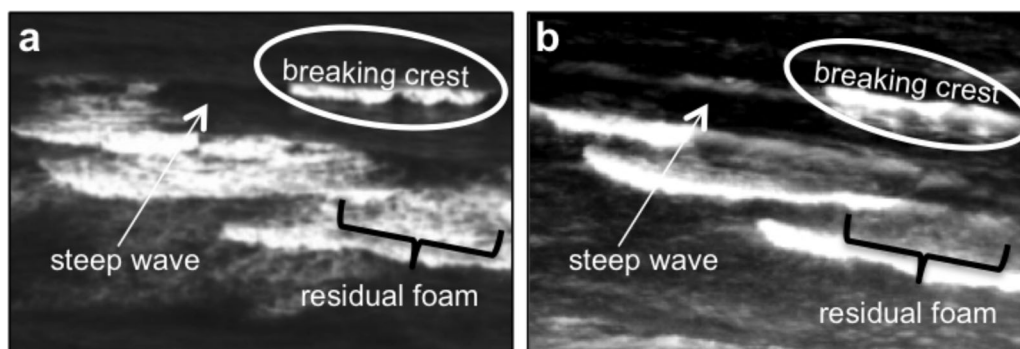


Figure 1. Comparison of simultaneous (left) visible and (right) infrared imagery of breaking waves in the surf zone. Active and residual foam both appear bright in the visible, while in the infrared, the breaking waves crests appear significantly brighter than the residual foam. Images adapted from Branch *et al.* [2014].

Here methods exploit the difference in the thermal signature of active and residual foam to identify and extract the crest-perpendicular length of the aerated breaking region, known as the roller length [Csanady, 2001], from IR imagery of the surf zone. The roller lengths are used to estimate wave breaking energy dissipation using the Duncan [1981] wave roller model, hereafter referred to as D81. D81 used the roller cross-sectional area and wave face slope to parameterize the energy dissipation due to wave breaking in the laboratory. With the observation that the cross-sectional roller area for all waves had the same aspect ratio, D81 was able to formulate the dissipation in terms of the crest-perpendicular length, wave slope, and void fraction of the breaking region.

Following its introduction by Duncan [1981], the concept of wave rollers as a mechanism for energy dissipation in wave breaking was adopted fairly quickly in modeling studies of the surf zone. Svendsen [1984a, 1984b] employed D81 in a simulated laboratory flume and found good agreement with the laboratory data. Later, the work of Stive and De Vriend [1994] refined the roller parameterization to include a dynamic roller model to allow for the slow transfer of wave energy into the roller as a wave broke across the surf zone. One of the perceived benefits of employing wave rollers in dissipation modeling arose when analyzing longshore currents in the field where the peak current was often strongest in the region shoreward of the maximum in wave breaking [Church and Thornton, 1993; Reniers and Battjes, 1997]. Because the roller delayed the transfer of stress from the wave motion to the underlying water, it was used as a mechanism to shift the wave forcing shoreward of the bar and away from the peak in breaking. The field application of the roller model of Stive and De Vriend [1994] was used by Ruessink *et al.* [2001] to predict longshore current profiles at Duck, NC and at Egmond beach in the Netherlands. The inclusion of rollers shifted the shape of the longshore current profile and improved prediction, but required adjustment of the roller model parameters. Additionally, the wave roller has been included in more complex models of circulation and sediment transport [for example, Warner *et al.*, 2008; Reniers *et al.*, 2004] without direct validation of D81 against dissipation rate measurements in the field.

Here IR imagery collected at the U.S. Army Corps of Engineers Field Research Facility (FRF) in Duck, NC, is used to remotely estimate energy dissipation due to wave breaking in the surf zone, which is compared with independent turbulent dissipation rate estimates. This paper is organized as follows: first, the IR signal of the sea surface and the role of wave breaking in the surf zone energy balance are introduced. Then, the D81 parameterization and the wave dissipation model by Janssen and Battjes [2007], hereafter referred to as JB07, are reviewed. The methods for IR image processing and the development of the retrieval algorithm for roller length are presented in detail, along with review of an in situ method for turbulent dissipation rate estimation. Finally, the D81 wave dissipation rate estimates are compared to the in situ turbulent kinetic energy (TKE) dissipation rate estimates, the JB07 dissipation rate estimates, and the bulk wave energy flux estimates. The underlying assumptions, sources of error, and implications are discussed. To the authors' knowledge, this is the first time thermal infrared imagery has been used to estimate wave roller geometric parameters and the first time the D81 model of wave energy dissipation has been tested in the field.

1.1. Thermal Signal of the Sea Surface

A thermal infrared camera is a passive sensor that collects emitted and reflected radiation along its look-path within a given wavelength band. Because objects emit thermal radiation at the range of earth ambient

temperatures, it can collect useful data during the day or night. The signal of the ocean surface received by the IR sensor can be described by a simplified radiative transfer equation, where the IR radiation received at the sensor is composed of emitted and reflected components from the sea surface according to,

$$\ell_{\text{meas}} = \varepsilon(\alpha)\ell_{\text{sea}} + \varrho(\alpha)\ell_{\text{sky}}(\alpha), \quad (1)$$

for a given wavelength. Here, α is the incidence angle and ℓ is the radiance (subscripts refer to measured, emitted by the sea surface, or reflected from the sky). Emissivity $\varepsilon(\alpha)$ and reflectivity $\varrho(\alpha)$ of sea water vary with incidence angle, such that as α increases from nadir to near-grazing, emissivity decreases [Masuda *et al.*, 1988]. By conservation of energy, the sum of the fraction of radiation transmitted, absorbed, and reflected must be unity. There is no transmission term in (1) because the sea surface is opaque to IR radiation. The emission term in (1) has replaced the absorption term, under the assumption that the sea surface is in thermodynamic equilibrium and Kirchoff's law of thermal radiation applies. The assumption that the sea surface absorbs and emits in equilibrium has been tested and verified [Masuda, 2006]. Therefore, the radiative energy balance for the sea surface reduces to,

$$\varepsilon(\alpha) + \varrho(\alpha) = 1, \quad (2)$$

and (1) can be rewritten as a function of emissivity alone,

$$\ell_{\text{meas}} = \varepsilon(\alpha)\ell_{\text{sea}} + (1 - \varepsilon(\alpha))\ell_{\text{sky}}(\alpha). \quad (3)$$

It is the dependence of emissivity on incidence angle that permits an IR imager to “see” waves. For a camera obliquely viewing the surf zone from a distance, and at moderate to large incidence angles ($\geq 60^\circ$), a small change in the local incidence angle due to wave slope produces a significant change in emissivity and thus a measurable change in radiance. A consequence of the angular dependence of ε is that lower emissivity in the far field causes the sea surface to appear cooler, even though its kinetic temperature may be uniform.

The incidence angle dependence of $\ell_{\text{sky}}(\alpha)$ may vary due to the atmosphere and cloud cover. For uniformly clear skies, the sea surface reflects a cool sky background, $\ell_{\text{sky}} \ll \ell_{\text{sea}}$. For uniformly cloudy skies, the sea surface reflects a warm cloud-covered background, $\ell_{\text{sky}} \approx \ell_{\text{sea}}$, as can happen for low-lying clouds, and (3) implies $\ell_{\text{meas}} \approx \ell_{\text{sky}}$. Thus, fully overcast conditions result in decreased contrast of a wavy sea surface signal. For partly cloudy skies, the background signal varies with α , and a small change in α may be the difference between observing the sea surface reflecting a cool sky background or a warm cloud-covered background. The contrast between the signal of breaking waves and the undisturbed sea surface is strong for clear sky conditions. However, when the sea surface signal includes the reflection of a warm, cloudy sky, the contrast between breaking waves and the undisturbed sea surface decreases.

At near-grazing incidence angles, breaking waves appear warm in IR because foam has a higher emissivity than nonfoamy water. This effect has been shown by Niclos *et al.* [2007] to hold whether the sea surface is considered a diffuse or specular reflector. Newer data have extended this relationship to 85° incidence angle [Branch *et al.*, 2012], and the resulting emissivity curves were found in agreement with those from Niclos *et al.* [2007]. The higher emissivity of foam causes foam produced by an actively breaking wave to have a higher apparent temperature than the undisturbed sea surface. Residual foam in the wake of a breaking wave cools quickly [Marmorino and Smith, 2005]. This change in kinetic temperature causes residual foam to appear cool (dark) in the IR imagery. The exact mechanism through which foam cools quickly has not yet been explained, but enhanced heat loss is likely due to the increased surface area and spray generation in foamy seas. The distinct IR signals of active and residual foam can be used to differentiate active breaking wave rollers from passive foam in IR imagery.

1.2. Energy Budget in the Surf Zone

The cross-shore gradient of wave energy flux, \mathcal{F} , in the surf zone is balanced by energy transferred via bottom drag ϵ_{bot} , wave breaking ϵ_{brk} , and reflection R , according to:

$$(1 - R) \frac{d\mathcal{F}}{dx} = \epsilon_{\text{brk}} + \epsilon_{\text{bot}}. \quad (4)$$

This balance neglects alongshore depth variations, nonlinear effects, and directional wave spreading. Reflection at the Field Research Facility at Duck, NC, varies with tidal stage from less than 3% to 18%, with

maximum reflection found during high tide for low wave heights (beach steepness increases with water stage) [Elgar and Herbers, 1994]. Turbulent energy production and dissipation are in balance near the bed and both are 2 orders of magnitude smaller than the depth-averaged rate of energy loss due to depth-limited breaking [Trowbridge and Elgar, 2001].

Dissipation due to wave breaking can be further divided into components of turbulent kinetic energy dissipation ϵ_{TKE} , bubble production and buoyancy ϵ_{buoy} , losses to the mean current ϵ_{mc} , sediment suspension and transport ϵ_{sed} , sound production ϵ_{sound} , heat production ϵ_{heat} , and sea spray production ϵ_{spray} [Lamarre and Melville, 1991; Bryan et al., 2003; Gerbi et al., 2009; Feddersen, 2012; Grasso et al., 2012; Lanckriet and Puleo, 2013]:

$$\epsilon_{brk} = \epsilon_{TKE} + \epsilon_{buoy} + \epsilon_{mc} + \epsilon_{sed} + \epsilon_{sound} + \epsilon_{heat} + \epsilon_{spray}. \quad (5)$$

ϵ_{TKE} and ϵ_{buoy} are coupled because bubbles that are injected into the water column contribute to turbulent mixing as they rise. ϵ_{TKE} , ϵ_{mc} , and ϵ_{sed} are energy transformations that occur at depth, while ϵ_{spray} occurs at the surface. ϵ_{buoy} , ϵ_{sound} , and ϵ_{heat} occur throughout the water column and at the surface. Since these components are difficult to measure individually, the bulk energy dissipation due to wave breaking $d\mathcal{F}/dx$ is often estimated based on wave height transformation measurements across the surf zone [Elgar et al., 1997] or by using offshore wave height and nearshore bathymetry to model wave height evolution across the surf zone [Collins, 1970; Battjes, 1972; Kuo and Kuo, 1974; Battjes et al., 1978; Thornton and Guza, 1983].

Apart from ϵ_{TKE} , most of the wave breaking energy pathways are neglected, with the assumption that they are small and hard to measure. Although turbulent dissipation rates measured in the surf zone under breaking waves have been shown to correlate with wave energy fluxes [Feddersen, 2012; Thomson, 2012], these studies cannot account for more than a small fraction of the energy input by wave breaking. This is at least partly due to the fact that ϵ_{TKE} is typically measured below the wave trough using acoustic current meters, so estimates may be biased low, missing the significant energy in the near-surface and wave roller.

1.3. Duncan [1981] Wave Roller Dissipation Model

Duncan [1981] proposed a single wave model of wave energy dissipation due to breaking as a balance between the shear stress, τ , along the breaking boundary, L_r , and the tangential component of the weight of the aerated breaking region of cross-sectional area, A , on the underlying wave face (equation (7) in D81):

$$\tau L_r = \rho' g A \sin \theta, \quad (6)$$

where ρ' is the density of the aerated breaking region and θ is the slope of the breaking wave face. This formulation was derived by combining the spatially integrated and time-averaged vertical and horizontal momentum equations over the breaking region. In the D81 experiments, a hydrofoil was towed through a flume and physical parameters related to the resulting breaking wave were measured. These breaking waves were considered fully developed and breaking in a steady state. Wave speeds were recorded between 0.625 and 1.03 m s⁻¹, wavelengths ranged 0.24–0.68 m, and wave face slopes measured 10°–14.7°. D81 found the geometry of the breaking region defined by A to be empirically self-similar by showing that the measured aspect ratio, A/L_r^2 , was essentially constant for all waves. That is, the ratio of the average thickness, A/L_r , to the roller length, L_r , was given by,

$$\frac{\text{thickness}}{\text{length}} = \frac{A/L_r}{L_r} = \frac{A}{L_r^2} = 0.11 \pm 0.01, \quad (7)$$

which allows A to be eliminated from (6). The D81 parameterization in (6) and (7) provides a powerful framework for estimating energy dissipation due to wave breaking, ϵ_{brk} in (5), on a wave-by-wave basis. Dividing the wave energy dissipation due to breaking by a time scale, T (wave period), yields the phase-averaged wave energy dissipation rate due to breaking,

$$\epsilon_{D81} = \frac{1}{T} 0.11 \rho' g L_r^2 \sin \theta, \quad (8)$$

where ρ' is the wave roller density.

Previous work by Haller and Catalan [2009] examined wave rollers in a freshwater laboratory wave tank experiment using visible imagery and in situ measurements. They used the D81 wave energy dissipation

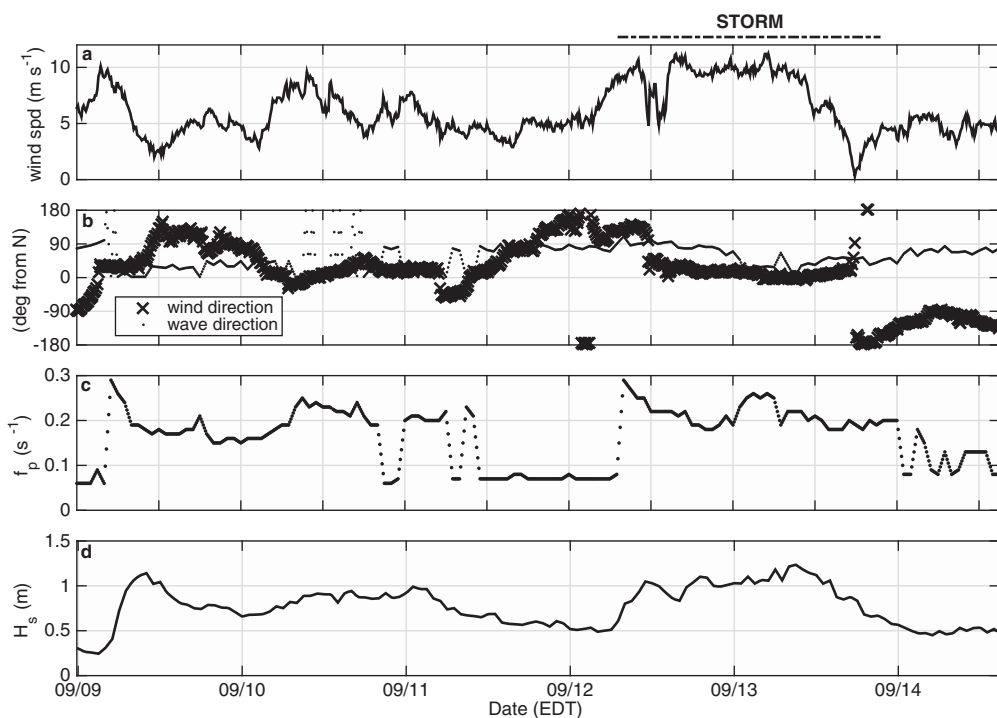


Figure 2. Conditions from the FRF at Duck, NC for the SZO experiment (9–15 September 2010): (a) wind speed, (b) wind (crosses) and wave (circles) direction, (c) peak wave frequency, and (d) significant wave height. The storm, from about noon on 12 September 2010 to 13 September 2010, is indicated.

formula to predict wave height from camera-based roller length estimates and compared the results to measured wave height across the surf zone. Results were promising over the limited range of waves produced, and although no direct estimate of wave energy dissipation is made with the laboratory data, the authors suggest that the D81 parameterization could be used to estimate wave dissipation in the field.

2. Methods

2.1. Experimental Setup

Image data were collected during the Surf Zone Optics (SZO) field campaign, 9–15 September 2010, at the Field Research Facility (FRF), which is operated by the U.S. Army Corps of Engineers at Duck, NC. A right-handed coordinate system is used at the FRF and is defined with the positive x axis pointing offshore, the positive y axis pointing northward and parallel to the shore, and the positive z axis pointing upward. The FRF y axis is oriented approximately 17° west of north. The shoreline position is approximately at $x = 100$ m. The beach morphology at Duck is variable, but typically includes a shore-parallel sand bar or terrace, and is often punctuated by rip current channels [Plant *et al.*, 1999]. Significant wave height, H_s , at the FRF is commonly 0.2–1.0 m, increases to 2–3 m during storms, and sometimes reaches as high as 4–5 m [Birkemeier *et al.*, 1985]. Figure 2 shows wave and weather conditions throughout the SZO experiment. The average H_s was 0.77 m, with a maximum of 1.24 m. Storm conditions on 12–13 September 2010 are indicated by sustained elevated wind speed, H_s , and wave frequency.

A cooled thermal IR camera (Indigo Phoenix) was mounted at the top of the 120 foot FRF imaging tower. The IR camera resolution is 640×512 and the spectral response range is 8–9.2 μm . The manufacturer's specified noise equivalent differential temperature (NEDT) is 25 mK. The camera has a 37° horizontal field of view (FOV) and was mounted to the tower at an incidence angle of 77.8° from nadir. Full frame data were collected at 10 Hz.

A 2 MHz Nortek Aquadopp acoustic Doppler current profiler (ADCP) was moored to the seabed at $(x, y) = (190 \text{ m}, 700 \text{ m})$, in the camera's FOV. The ADCP was sampled at 1 Hz from 35 vertical bins, every 10 cm vertically. At high tide, 30 of the bins were submerged. At low tide, a minimum of five submerged bins were

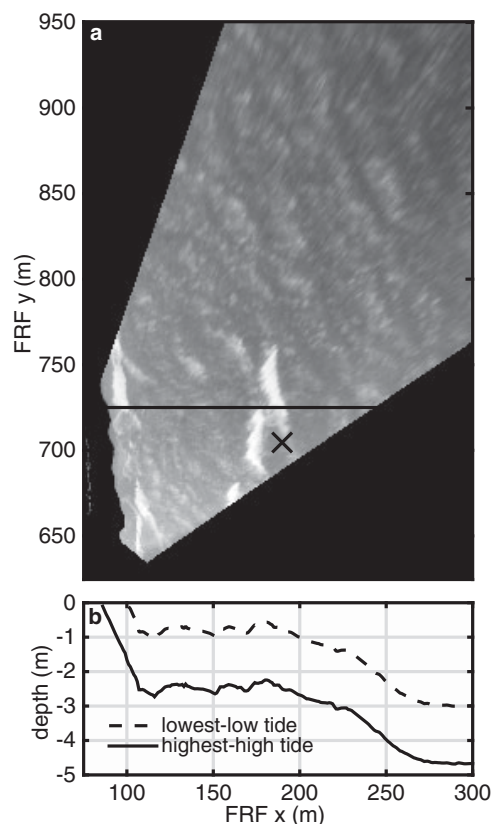


Figure 3. (a) Example of the rectified IR camera field of view in the FRF coordinate system. The transect (line) and location of the moored ADCP (cross) are marked. (b) Transect bathymetry from FRF survey on 6 September 2010, shown with minimum and maximum tidal elevation measured during the experiment.

lower left of the timestack. As expected from the bathymetry (Figure 3b), depth-limited breaking occurs over the terraced-bar (hereafter referred to as the bar or sand bar, for simplicity) and at the shore.

Eighteen minute timestacks were created at the start of every half hour. Shortened timestacks, due to truncated recording, were discarded. Prior to analysis to identify breaking wave rollers, the shore and dunes were removed from the timestack and the background pixel intensity was temporally and spatially normalized with minimal reduction of contrast between the background and features of interest (i.e., breaking waves). Each raw timestack $I(x, t)$ was temporally normalized by removing a background intensity at each time step,

$$\tilde{I}(x, t_j) = I(x, t_j) - I_{25}(t_j), \quad j = 1, \dots, N_t, \quad (9)$$

where $I_{25}(t_j)$ is the intensity of the 25th percentile of the spatial cumulative distribution function (cdf) created from the transect at time t_j . The cdf of $\tilde{I}(x, t)$ was then computed at each x -location, and the pixel intensity of the fifth percentile of the temporal cdf, $\tilde{I}_5(x_i)$, was removed from all the data at the respective x -location following,

$$\hat{I}(x_i, t) = \tilde{I}(x_i, t) - \tilde{I}_5(x_i), \quad i = 1, \dots, N_x. \quad (10)$$

The 25th and 5th percentile intensities were chosen based on manual comparison of several timestacks. Finally, the pixel intensity range of each timestack was shifted by subtracting the global minimum value of $\hat{I}(x, t)$,

$$I(x_i, t_j) = \hat{I}(x_i, t_j) - \min[\hat{I}(x, t)]. \quad (11)$$

required for analysis. This criteria was only violated once (lower-low tide on 9 September 2010). ADCP pressure data are used to measure wave height, from which an estimate of wave slope was calculated for use in (6). ADCP velocity data are used to calculate an in situ estimate of turbulent kinetic energy dissipation rate, ϵ_{moored} , which is compared to the remotely derived estimates of energy dissipation rate due to wave breaking. Additional wave data were collected from the FRF ADCP moored in approximately 3 m water depth at $(x, y) = (245 \text{ m}, 893 \text{ m})$.

SWIFT drifters [Thomson, 2012] were released in the area and allowed to drift through the IR field of view. Turbulence data collected onboard these drifters are used to calculate additional estimates of the turbulent kinetic energy dissipation rate, ϵ_{SWIFT} , which have less measurement noise than the fixed ADCP.

2.2. Image Processing Techniques

2.2.1. Image Data Normalization

Cross-shore transects of the surf zone were extracted from the IR images for analysis. The transects extended from $x = 85 \text{ m}$ to $x = 245 \text{ m}$, passing over the trough-bar bathymetry along $y = 725 \text{ m}$, with 0.25 m spacing. A rectified IR image is shown in Figure 3 with the nearshore ADCP marked by a black "x," the transect marked as a black line, and its bathymetry given in the panel below. A sample of the IR data is shown in the timestack in Figure 4, where intensity along the transect from each frame is stacked sequentially. Actively breaking wave crests appear as bright streaks traveling onshore from the upper right to the

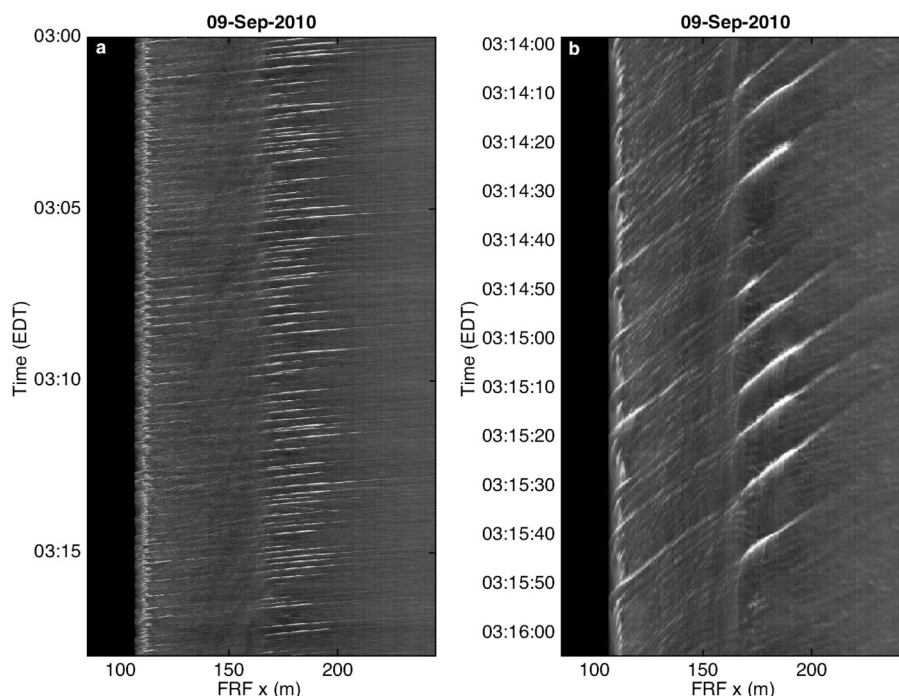


Figure 4. (a) Timestack of IR imagery created from 18 min of data along the transect shown in Figure 3. Time increases from top to bottom and x increases to the right (shoreline at $x = 110$ m). (b) An expansion of 2 min of data shows bright breaking waves over the bar ($x = 190$ m) and at the shoreline. Other passing waves appear as oblique ridges of lesser intensity.

2.2.2. Wave Roller Identification

Figure 5 shows a series of snapshots taken throughout the passage of a breaking wave, each accompanied by its instantaneous and 10 min probability density function (pdf). Each pdf was created from the pixel intensities observed within the sample region marked by the black square (covering approximately 4 m^2), chosen to ensure that the IR signals of a breaking wave, residual foam, and background water, were individually sampled. This time series illustrates the increased intensity of a passing wave roller followed by its wake of cool, low-intensity, residual foam, as well as a low-intensity quiescent wave state.

The 10 min IR intensity distribution is typically bimodal, with a small narrow peak at high intensities due to actively breaking waves (Figures 5a and 5e) and a large broad peak at low intensities due to background water and cooling/cool foam (Figures 5b, 5c, 5f, and 5g). The final snapshot-histogram pair (Figures 5d and 5h) shows a nonbreaking wave. The steep wave face appears warm because the decreased incidence angle at which the sea surface is observed increases the signal received by the IR imager. However, comparing histograms (h) and (e), the nonbreaking wave face does not achieve pixel intensities as high as the breaking wave. The dramatic distinction between the infrared signal of breaking waves and the rest of the distribution, as seen in the 1 s distribution in Figure 5a, suggests thresholding may be sufficient to identify active wave rollers.

The goal is to objectively choose a threshold at or near the local minimum between the two peaks of the bimodal distribution, which is present in the vast majority of the timestacks produced. However, for a small fraction of measurements, the small peak at high intensities due to breaking waves is not present; instead, it is replaced with a long tail or plateau, here called a “unimodal-plateau” distribution. While there are still breaking waves with high pixel intensities, the breaking rate is not sufficient to develop a second peak. The detection algorithm was designed to work on both types of intensity distributions and also includes a secondary method for sample times when environmental conditions resulted in an irregular intensity distribution that could not be sufficiently counteracted by the previously described normalization procedure.

A threshold was chosen based on the first or second-order differences (discrete derivatives) of the pdf $p(\mathbf{I})$, as,

$$p'(\mathbf{I}) \equiv \frac{\Delta p(\mathbf{I})}{\Delta \mathbf{I}} = \frac{p(\mathbf{I}) - p(\mathbf{I}-1)}{\mathbf{I} - (\mathbf{I}-1)}, \quad \mathbf{I} = 1, \dots, N_I, \quad (12)$$

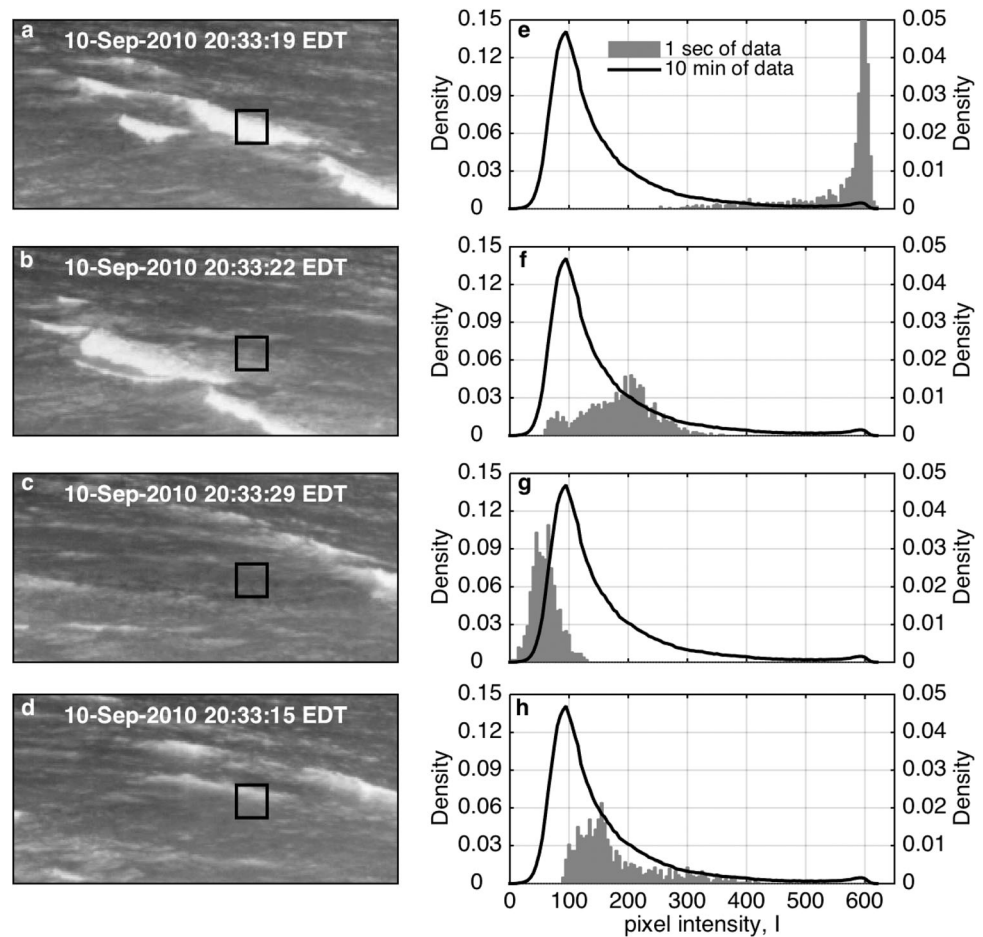


Figure 5. A series of IR snapshots and corresponding pixel intensity pdfs. The outlined sample region in each IR image contains (a) a breaking wave, (b) residual foam, (c) cool, residual foam, and (d) a quiescent wave state. (e–h) The gray pdf (left y axis) is the instantaneous distribution created from a 1 s record corresponding to the accompanying image. The black pdf (right y axis) is the same in all plots and was created from a 10 min record.

$$p''(I) \equiv \frac{\Delta p'(I)}{\Delta I} = \frac{p'(I) - p'(I-1)}{I - (I-1)}, \quad I=2, \dots, N_I. \quad (13)$$

$p'(I)$ describes the rate of change, or slope, of $p(I)$, and $p''(I)$ describes the curvature of $p(I)$. When a bimodal $p(I)$ was present, as in Figure 6a, the threshold, I_b , was chosen as the pixel intensity of the first zero up-crossing of $p'(I)$ that follows the intensity of the global minimum of $p'(I)$, I_{\min} . Using this method, the breaking threshold intensity was defined as,

$$p''(I_b) = 0, \quad I_b > I_{\min}. \quad (14)$$

If I_b was not defined (the case for unimodal-plateau distributions, as in Figure 6b) or was equal to N_I , the maximum pixel intensity observed in $p(I)$, the second derivative $p''(I)$ was used to determine a threshold. The second local maximum of $p''(I)$ indicates the pixel intensity at which the curvature of $p(I)$ achieves maximum positive concavity subsequent to the modal peak in the distribution,

$$p''(I_{\max}) = \max(p''(I > I_{\min})). \quad (15)$$

The breaking threshold was then objectively chosen as the intensity corresponding to the 25th percentile of the set of $p''(I)$ with intensity greater than I_{\max} ,

$$p''(I_b) = [p''(I > I_{\max}) > 0]_{25}. \quad (16)$$

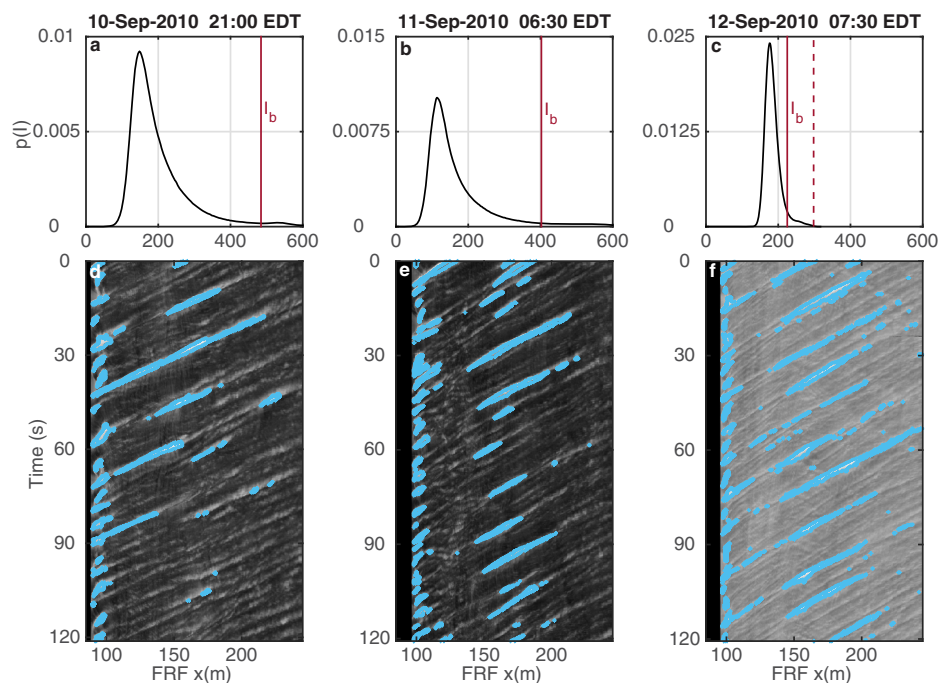


Figure 6. Three examples of threshold algorithm results. Normalized (a) bimodal, (b) unimodal-plateau, and (c) inhomogeneous background intensity distributions. $p(I)$ marked at threshold I_b with a red line. For Figure 6c, both the threshold chosen using the zero up-crossing method (dashed) and the $p''(I)$ method (solid) are shown. (d–f) Two minute segments of the timestacks of IR imagery, from which $p(I)$ in Figures 6a–6c were created, with identified breaking waves outlined in blue.

After determining I_b using one of these two methods, the normalized timestacks were converted to binary masks, $M(x, t)$, by setting all pixels whose value equaled or exceeded I_b to one and all pixels whose value was less than I_b to zero.

A quality control protocol consisting of visual and automated inspection was employed to ensure that a reasonable threshold was chosen. In some cases where I_b was chosen via the zero up-crossing method (14), I_b was set too high, and not all breaking waves were identified. The poor performance of the detection algorithm in cases like this one was attributed to unusual behavior of $p(I)$ or failed normalization due to nonuniform reflected sky conditions. Detection algorithm failure was assumed if the percentage of pixels identified as active foam in a given timestack was less than 0.3%. This percentage is slightly less than that expected if the timestack exhibited only shore break, as assessed through manual inspection of the data. If this occurred, then a new threshold was chosen via the $p''(I)$ method (16), and a new binary mask was created. In Figure 6c, the dashed and solid red lines show the I_b chosen by the zero up-crossing and $p''(I)$ methods, respectively. The breaking rate and roller length statistics for timestacks reprocessed with the secondary thresholding method were similar to those with bimodal pixel intensity distributions and thresholded with the zero up-crossing method. Therefore, no further quality control protocols were deemed necessary.

Lastly, basic image processing techniques were used to refine the binary masks. Spurious values were removed if the pixel set to 1 was surrounded by values of 0. Isolated zeros in the binary mask were filled if they were surrounded by values of 1. If the eight-cell neighborhood around a pixel set to 0 contained at least five values of 1, then that pixel was changed to 1. Erosion and dilation image processing techniques were avoided in order to best preserve the dimensions of the identified regions used for roller length. Further detail on the image processing methods is given by Carini [2014].

A sensitivity analysis was performed on the three timestacks in Figure 6 to demonstrate the effect of a change in threshold value for actively breaking waves. Figures 6a and 6d show the typical bimodal intensity distribution, Figures 6b and 6e show a unimodal-plateau intensity distribution, and Figures 6c and 6f illustrate how inhomogeneous background intensity complicates the choice of a single threshold to be used

Table 1. Change in Percent Coverage (ΔPC) for 25% Increase and Decrease in I_b

Example Pdf	I_b	I_{max}	PC_{I_b}	$\Delta PC_{+25\%}$	$\Delta PC_{-25\%}$
Bimodal	484.5	697	2.06%	-1.78%	+3.17%
Unimodal-plateau	402.5	679	3.95%	-3.05%	+4.84%
Inhomogeneous background	225.0	317	4.39%	-3.86%	+24.58%

over the entire timestack. The ratio of the number of pixels identified to the total number of pixels in the timestack, or the percent coverage (PC), was used as a sensitivity assessment statistic. The detection algorithm is considered robust if a small change in threshold intensity, I_b , produces a small change

in PC. For each example, the change in percent coverage was computed for a 25% change in the threshold value as,

$$\Delta PC_{\pm 25\%} = PC_{I_b \pm 0.25 I_b} - PC_{I_b} \quad (17)$$

The sensitivity analysis results, summarized in Table 1, show decreased PC for increased threshold choice and increased PC for decreased threshold choice, as expected. Both $\Delta PC_{\pm 25\%}$ and $\Delta PC_{-25\%}$ are small (<5%) for all but the inhomogeneous background case, where $\Delta PC_{-25\%} = 24.58\%$. The inhomogeneous background case represents a minority of the data (17%), and manual examination reveals that the normalization of pixel intensity (processing common to all data) reduces the contrast between wave rollers and background water in these cases, which causes increased sensitivity to threshold choice. These cases occurred predominantly during the storm, from about noon on 12 September 2010 to 13 September 2010, when elevated wind speed increased the breaking rate. For the remaining 83% of the data analyzed, the mean $|\Delta PC_{\pm 25\%}|$ is 3.21%, which demonstrates the robust nature of the presented thresholding routine for IR imagery.

Of 253 valid timestacks recorded, 210 were processed using the primary thresholding routine and 43 were processed using the secondary thresholding routine. Those cases needing secondary thresholding occurred mainly during storm conditions. The breaking rates (number of breakers/18 min) over the bar and at the shoreline calculated from the binary masks are comparable to the most energetic wave frequencies measured by the FRF 3 m ADCP. A comparison of the full wave energy-frequency spectrum and the maximum breaking rate at the shoreline and at the bar (maximum value averaged with its four nearest neighboring cross-shore pixels) is shown in Figure 7. The shore breaking rate agrees well with the sea frequency, and the bar breaking rate agrees with the swell and infragravity frequencies, although both breaking rates fluctuate tidally. Modulation of breaking rate over the bar is governed by water depth. At low tide, waves shoal to some sufficient wave steepness and break, while at high tide, fewer waves reach the depth-limited steepness needed to induce breaking. This results in instances of a measured breaking rate that is less than the dominant swell or sea frequencies. At the shore, tidal modulation of breaking

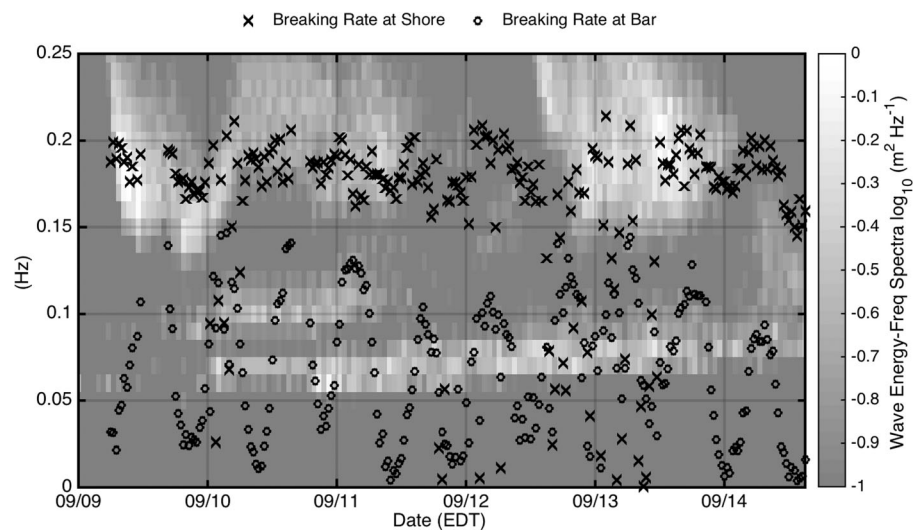


Figure 7. Time series of the mean breaking rate following the shoreline (crosses) and at the bar (circles) plotted over the wave energy-frequency spectrum computed from the FRF 3 m ADCP for the full experimental record.

rate may be a consequence of increased reflection, and therefore decreased breaking, due to the steepened beach at high tide.

2.2.3. Roller Length Estimation

To obtain the projected roller length L'_r , a forward difference with respect to space was taken at every time step, $dt = 0.1$ s, of the binary masks. The front edge, or toe x_{toe} , of a breaking wave was indicated every time the forward difference produced a value of 1. The trailing edge, or crest x_{crest} , of a breaking wave was indicated each time the forward difference produced a value of -1 . The cross-shore position of each breaking wave at time t , x_b , was defined by the midpoint between its toe and crest positions. Therefore, the projected roller length was defined as,

$$L'_r(x_b, t) = x_{\text{crest}} - x_{\text{toe}}, \quad (18)$$

where, $x_b = (x_{\text{crest}} + x_{\text{toe}})/2$.

The projected roller length was corrected for image misregistration due to the wavy water surface. The correction is a function of wave position in space, wave slope, and wave direction. The vertical position (z) was approximated by mean sea level (MSL), calculated based on the tidal elevation for each 18 min timestack (estimated using the pressure measurement from the ADCP at $x = 190$ m). *Duncan* [1981] assumes that the toe of the roller is not in the trough of the wave, but rather some distance up the wave face, approximately at mean water level. Therefore, here it was assumed that the three-dimensional position of the toe of the wave roller was correctly identified at $(x, y = 725 \text{ m}, z = \text{MSL})$ and can serve as a reference point, \vec{r}_1 .

From \vec{r}_1 , the projection of the roller length, \vec{r}_2 , was defined as,

$$\vec{r}_2 = \vec{r}_1 + [L'_r, 0, 0]. \quad (19)$$

The line, \vec{l} , that begins at the camera's position, \vec{r}_{cam} , passes through the true breaking wave crest, \vec{r}_{crest} , and ends at \vec{r}_2 , can be written as,

$$\vec{l} = \vec{r}_{\text{cam}} + s(\vec{r}_2 - \vec{r}_{\text{cam}}), \quad s = [0 : 1], \quad (20)$$

where s is a variable increased from 0 to 1 to create the line from \vec{r}_{cam} to \vec{r}_2 . Figure 8 illustrates this geometry and identifies wave roller slope, θ (see section 2.3 for details of wave slope estimation), and wave direction relative to the camera look-direction, ϕ (from FRF Aquadopp in 3 m water depth). In order to find \vec{r}_{crest} , the intersection of \vec{l} and the wave face was identified. The wave face was defined as,

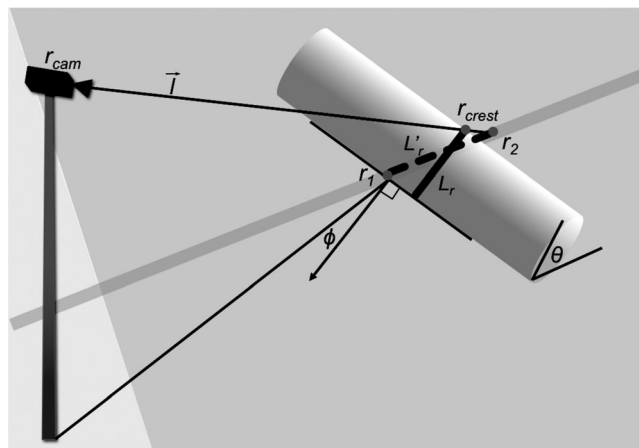


Figure 8. Schematic of camera-wave geometry. The position of the camera in (x, y, z) -space is denoted by r_{cam} . The position of the toe of the wave along the cross-shore transect is marked by r_1 , and the intersection of the camera's line of sight \vec{l} and the wave crest is marked by r_{crest} . The projected roller length L'_r is the distance $r_2 - r_1$, and the corrected roller length L_r is the crest-perpendicular length of the breaking region descending from r_{crest} . The slope of the breaking wave is denoted by θ and its propagation direction by ϕ .

$$z_{\text{int}} = r_{1,z} - \frac{dz}{dx} r_{1,x} - \frac{dz}{dy} r_{1,y}, \quad (21)$$

where slopes dz/dx and dz/dy were defined as,

$$\frac{dz}{dx} = \tan \theta \cos \phi, \quad (22)$$

$$\frac{dz}{dy} = \tan(90 - |\phi|), \quad \text{and} \quad (23)$$

$$\frac{dz}{dy} = \frac{dz}{dx} \left(\frac{dy}{dx} \right)^{-1} = \frac{\tan \theta \cos \phi}{\tan(90 - |\phi|)}. \quad (24)$$

Setting equal (20) and (21) and solving for the point of intersection, t_{crest} , yielded,

$$t_{\text{crest}} = \frac{z_{\text{int}} - r_{\text{cam},z} + \frac{dz}{dx} r_{\text{cam},x} + \frac{dz}{dy} r_{\text{cam},y}}{(\vec{r}_2 - \vec{r}_{\text{cam}}) \cdot \left(-\frac{dz}{dx}, -\frac{dz}{dy}, 1 \right)}. \quad (25)$$

t_{crest} was then used in (20) to solve for \vec{r}_{crest} :

$$\vec{r}_{\text{crest}} = \vec{r}_{\text{cam}} + t_{\text{crest}}(\vec{r}_2 - \vec{r}_{\text{cam}}). \quad (26)$$

The distance from \vec{r}_1 to \vec{r}_{crest} is the corrected roller length, L_r :

$$L_r = \frac{r_{\text{crest},z} - r_{2,z}}{\sin \theta}. \quad (27)$$

The ratio of L'_r to L_r , Π , was computed:

$$\Pi = \frac{L'_r}{L_r} = \frac{L'_r \sin \theta}{r_{\text{crest},z} - r_{2,z}}. \quad (28)$$

The resultant corrected roller length is,

$$L_r = \frac{L'_r}{\Pi(\theta, \phi)}. \quad (29)$$

Here the wave slope ranges from 2° to 8° , and the wave direction relative to the camera look-direction ranges from 11° to 83° with an interquartile range of 33° – 61° . The wave propagation direction relative to the camera look-direction determines whether the roller length is a crest-perpendicular measurement or taken at an oblique angle to the crest. An obliquely measured roller length is larger than the actual roller length. For θ between 2° and 8° and ϕ less than 60° , $\Pi(\theta, \phi)$ ranges from 1 to 4. Implications of errors in L_r are addressed in section 3.2.

2.3. Wave Slope Estimation

For use in (8), an estimate of θ is computed for each 18 min timestack from the corresponding ADCP data. The ADCP pressure time series is converted to a sea surface height time series, $\eta(t)$, using linear wave theory. $\eta(t)$ is converted to $\eta(x)$ using an average shallow water phase speed, $c = \sqrt{gh}$ where h is the MSL. Each peak and its preceding trough are identified in $\eta(x)$. Individual wave heights are estimated as $\eta(x_{\text{peak}}) - \eta(x_{\text{trough}})$, and the trough to peak distance is computed for each individual wave as $x_{\text{peak}} - x_{\text{trough}}$. Wave slope for each wave is then defined as the angle formed by the ratio of the wave height to the cross-shore distance from trough to peak of each wave:

$$\theta_i = \tan^{-1} \left[\frac{\eta(x_{\text{peak},i}) - \eta(x_{\text{trough},i})}{x_{\text{peak},i} - x_{\text{trough},i}} \right]. \quad (30)$$

For each 18 min time series, the average wave slope is estimated from the subset of slopes produced by waves of height H_{rms} or greater, as waves meeting this height criterion are most likely to be breaking over the bar (ADCP location, $x = 190$ m), and their slope, therefore, serves as a proxy for the slope of an actively breaking wave in D81. Figure 9 shows these bulk wave slopes range from 1.8° to 7.6° , with a mean of 4.5° , and fall within the 2° – 24° range reported in the literature from both laboratory and field experiments [Duncan, 1981; Dally and Brown, 1995; Reniers and Battjes, 1997; Ruessink et al., 2001; Haller and Catalan, 2009]. The shaded region marks the minimum and maximum slopes produced by waves at least as high as H_{rms} observed within each 18 min time series of sea surface height. The estimated wave slope varies gradually over the experiment, thus using the mean wave slope for each 18 min record is reasonable for a first test of D81. The D81 dissipation rate is also estimated using constant wave slopes of 5° (experimental mean) and 20° (nearly the largest slope reported in the literature) in order to assess its sensitivity.

2.4. Duncan [1981] Estimate of Wave Dissipation Rate

Duncan's wave roller dissipation rate is estimated for each 18 min timestack on a wave-by-wave basis using each L_r observed at a given location and time and the average θ estimated from the corresponding sample time. Summing over time at each x -position and dividing by the record length, t_{total} , yields a wave dissipation rate estimate at each location,

$$\epsilon_{\text{D81}}(x) = \frac{1}{t_{\text{total}}} \sum_i 0.11 \rho' g L_{r,i}^2(x) \sin \theta. \quad (31)$$

The density of the aerated breaking region, ρ' , is set to 60% of the density of sea water [Duncan, 1981].

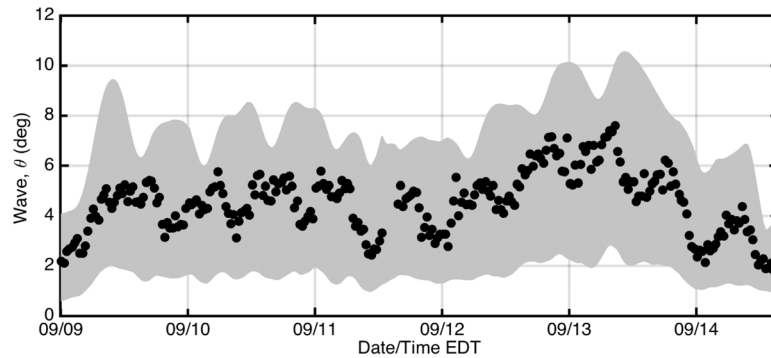


Figure 9. Mean wave slope estimates derived from the time series of surface displacement. One estimate was made for each 18 min series of data at the top of every half hour, and the gray band extends from the minimum to the maximum wave slope estimated in each 18 min series.

Error estimates for ϵ_{D81} due to the remote sensing measurements stem from uncertainty in the roller length and the wave slope θ . To represent this uncertainty, the minimum and maximum estimated wave slopes and the range of observed wave angles (waves approaching from 3 to 75° north of the FRF x axis) are used to compute the minimum and maximum values of corrected roller length for each observed breaking wave. Then the wave energy dissipation rate is calculated with these minimum and maximum roller lengths and wave slopes (wave slope constant for each 18 min timestack) via (31). This range of values brackets each original estimate of ϵ_{D81} (displayed as error bars in Figure 12). Wave slope is likely the parameter with the largest variance in this formulation. Therefore, to test the sensitivity of D81 to wave slope, a time-constant slope of 5° is used to calculate ϵ_{D81} instead of the measured wave slope. A mean difference of -7.6% indicates the new estimate is smaller than the original estimate. The mean difference increases to +33.3% when using a constant wave slope of 20° (nearly the largest reported in the literature [Duncan, 1981; Dally and Brown, 1995; Reniers and Battjes, 1997; Ruessink et al., 2001; Haller and Catalan, 2009]).

2.5. In Situ Estimation of TKE Dissipation Rate

In situ TKE dissipation rates are estimated from ADCP data using the methods developed in Wiles et al. [2006] and Thomson [2012]. Assuming the measured velocity fluctuations are isotropic and homogeneous and describe turbulent eddies within the inertial subrange, the second-order structure function, $D(z, r)$, is used to estimate TKE dissipation rate. In the inertial subrange, a cascade of energy from large scales to small scales relates the slope of $D(z, r)$ to the rate of dissipation ϵ . The second-order structure function is calculated using the velocity fluctuations, $v' = v - \bar{v}$, at each vertical position in the water column, z , for a range of separation distances, r , between the chosen z and the remaining vertical bins:

$$D(z, r) = \langle (v'(z) - v'(z+r))^2 \rangle. \tag{32}$$

The TKE dissipation rate is then estimated according to,

$$\epsilon = \left(\frac{D(z, r) - N}{C_v^2 r^{2/3}} \right)^{3/2}, \tag{33}$$

where N is an offset due to the Doppler noise in the ADCP velocity estimates and C_v^2 is a constant set to 2.1 [Wiles et al., 2006; Thomson et al., 2010].

This method is applied to both a bottom-mounted ADCP on the bar (Eulerian frame of reference) and a freely drifting SWIFT buoy (quasi-Lagrangian frame of reference) to estimate TKE dissipation rates, ϵ_{moored} and ϵ_{SWIFT} , respectively. Moored and drifting ADCP velocity data are processed in 5 min bursts to compute a time series of TKE dissipation rate depth profiles. Depth-integrating ϵ and then time-integrating (over 18 min time segments corresponding to the IR timestacks) gives the estimated total TKE dissipation rate at the ADCP's location for a given 18 min time period. The results from the fixed instrument on the bar, ϵ_{moored} , have a much higher noise floor (4 W m^{-2}), because the measurement is contaminated by wave orbital velocities and the instrument was in a noncoherent mode with relatively large (10 cm) bins. The results from the drifting SWIFT buoy, ϵ_{SWIFT} , have a much lower noise floor (0.1 W m^{-2}) because the platform is wave-following (and thus does not include the

wave orbital motions) and the instrument was in a pulse-coherent mode with smaller (4 cm) bins [Thomson, 2012].

3. Results and Discussion

3.1. Roller Length Distribution and Evolution

Two-dimensional histograms of the full record of L_r as a function of cross-shore position for three 18 min sample periods (low, mid, and high tide examples) are shown in Figure 10. In general, there are two peaks in the spatial distribution of L_r , a narrow peak at the shoreline and a broad peak over the sand bar. Overall, the highest occurrence of wave rollers is between $L_r = 0.5$ m and $L_r = 2.0$ m. The shore break exhibits roller lengths as great as 3.0 m, with an average of 0.75 m. The position of the shore break shifts onshore as the tidal elevation rises, but its cross-shore shape and density distribution remain consistent throughout the different tidal stages. The bar break reaches maximum roller lengths near 4 m. Like the shore break, the position of the bar break shifts onshore as the tidal elevation rises. However, the occurrence

of breaking waves over the bar decreases significantly with tidal elevation. Both the cross-shore shift and change in occurrence of breaking at the bar is dependent on water depth. During low tide, waves reach their critical steepness [Miche, 1944] and break farther offshore than at high tide.

At the low tide shown in Figure 10a, the spatial distribution of peak roller lengths suggests that waves begin to break offshore and grow to some depth-limited L_r before decreasing. At midtide (Figure 10b), the bar break is sparser and its spatial distribution is narrower than at low tide, but it maintains a similar shape. At high tide, there are so few breaking waves over the bar that individual breaker paths are distinguishable as continuous arcs of evolving L_r (specifically for $x = 120$ – 220 m in Figure 10c). Analysis of the complete data set shows that roller lengths reach as great as 4.5 m at the shore and 5.5 m over the bar.

3.2. D81 Wave Energy Dissipation Rates

For each 18 min timestack, the energy dissipation rate due to wave breaking, ϵ_{D81} , was calculated using (31) at each x -location along the transect. Figure 10d shows the cross-shore profile of ϵ_{D81} for the low, mid, and high tide examples from Figures 10a–10c. The dissipation rate estimate from the shore break is similar across the three examples because breaking frequency and roller length vary little with tidal stage. Over the bar, however, ϵ_{D81} decreases significantly from low to high tide, from $\mathcal{O}(10)$ to $\mathcal{O}(10^{-1})$ W m^{-2} , respectively.

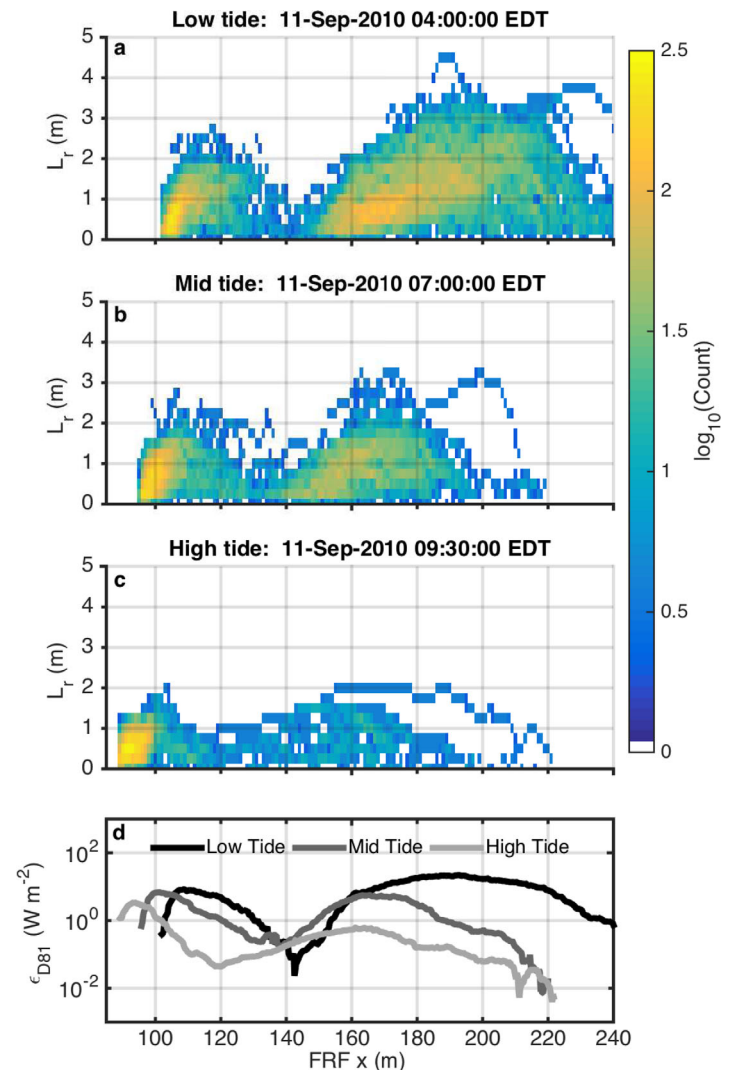


Figure 10. Two-dimensional histograms of roller length, L_r (m), as a function of cross-shore position. Examples shown from (a) low tide, (b) mid tide, and (c) high tide on 11 September 2010. (d) Cross-shore profiles of ϵ_{D81} computed from the roller lengths represented in the 2-D histograms above.

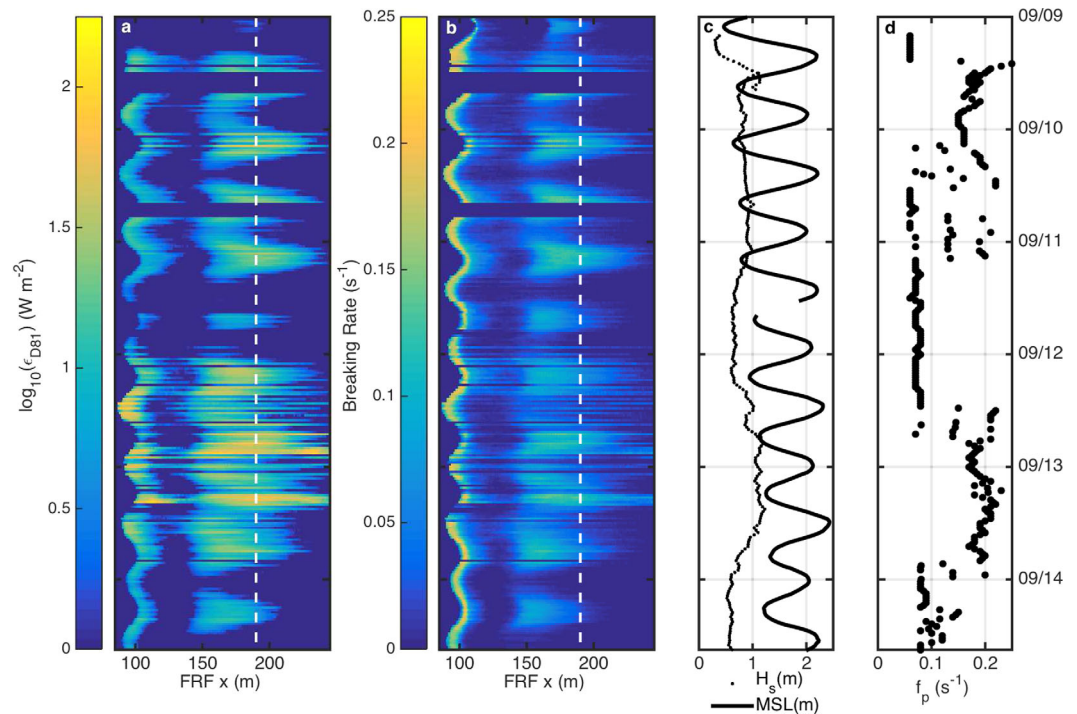


Figure 11. (a) Timestack of average wave dissipation rate as estimated using the D81 parameterization along the cross-shore transect, for the full experiment record. (b) Timestack of breaking rate as computed from the detection algorithm along the cross-shore transect, for the full experiment record. (c) Significant wave height time series (dotted) measured by the FRF 3 m ADCP, and mean sea level time series (solid) at cross-shore location $x = 190$ m (marked by white dashed line in Figures 11a and 11b) as measured by the ADCP on the sand bar. (d) Peak wave frequency from the FRF 3 m ADCP.

Cross-shore profiles of ϵ_{D81} from each 18 min timestack throughout the experiment are shown in Figure 11a. A timestack of cross-shore breaking rate, the MSL at $x = 190$ m and H_s , and f_p are provided for reference in Figures 11b–11d, respectively. The timestack of cross-shore profiles of ϵ_{D81} is clearly modulated by the tide and varies with breaking rate and H_s . Low tide corresponds to high breaking rates at the bar and large dissipation rates, and high tide corresponds to low breaking rates at the bar and small dissipation rates. It is clear that very low values of ϵ_{D81} correspond to breaking rates near zero (Figure 12c). In this case, the remote estimate is based on observation of very few waves, indicating it should be small and potentially noisy. Correspondence with H_s is best illustrated during and just after the storm. High H_s (~ 1.2 m) during the storm corresponds to values of ϵ_{D81} between 30 and 100 W m^{-2} . When H_s decreases to approximately 0.5 m poststorm, ϵ_{D81} decreases to 10 W m^{-2} or less.

3.3. Comparison of Wave Energy Dissipation Rates and In Situ TKE Dissipation Rates

The variation of the remote wave dissipation estimate is further examined at the cross-shore position of the ADCP ($x = 190$ m), where it can be compared with in situ estimates. Figure 12a shows the remotely estimated wave dissipation rate, ϵ_{D81} , spans almost 4 orders of magnitude with a maximum just less than 100 W m^{-2} and a minimum near 10^{-2} W m^{-2} . The time series of the in situ turbulent dissipation rate estimate, ϵ_{moored} , is also shown in Figure 12a. Error bars (95% confidence intervals based on instrument Doppler noise [Thomson *et al.*, 2010]) are shown for each estimate, and data below the noise floor for the moored ADCP, marked by horizontal gray dashed line at 4 W m^{-2} , are excluded from the ϵ_{moored} time series. The data gap on 11 September 2010 is due to equipment maintenance (battery replacement and data download).

As represented in (5), the wave energy dissipation due to breaking ϵ_{brk} transfers energy through many pathways, including turbulent kinetic energy dissipation. The D81 estimate is a measure of ϵ_{brk} , while ϵ_{moored} is a measure of ϵ_{TKE} . Therefore, while ϵ_{D81} and ϵ_{moored} should covary, they are not expected to balance. The values of ϵ_{moored} exhibit similar tidal fluctuations and comparable magnitude to ϵ_{D81} , but maintain a smaller

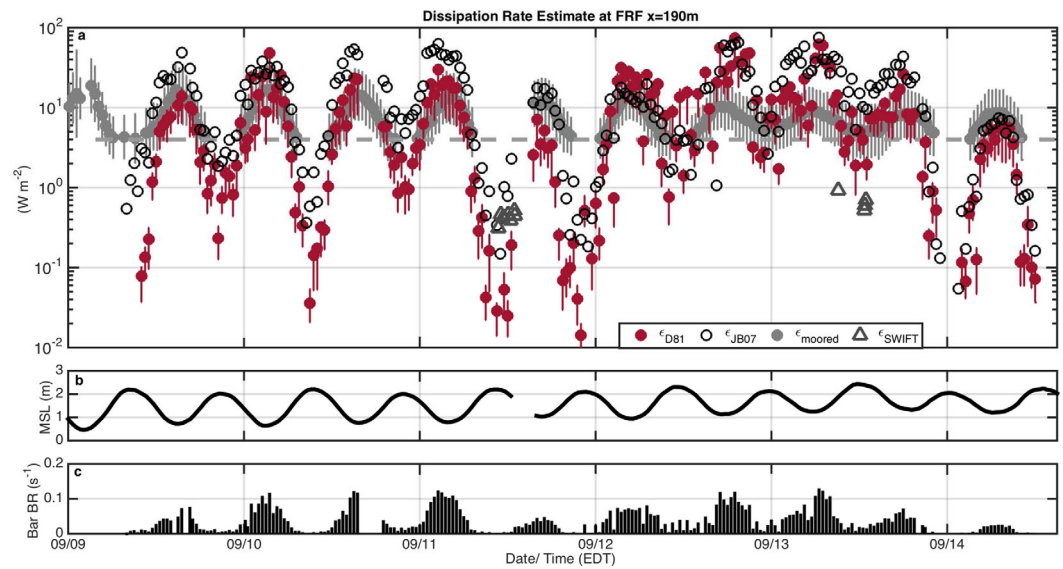


Figure 12. (a) Remote D81 wave dissipation rate estimate ϵ_{D81} (red circles with error bars) compared with in situ moored TKE dissipation rate estimate ϵ_{moored} (gray circles with error bars), SWIFT TKE dissipation rate estimates ϵ_{SWIFT} (gray open triangles), and the JB07 wave dissipation rate estimate ϵ_{JB07} (black open circles). The horizontal gray dashed line marks the noise floor of ϵ_{moored} at 4 W m^{-2} . (b) Mean sea level time series from ADCP at $x = 190 \text{ m}$. (c) Breaking rate time series from $x = 190 \text{ m}$.

dynamic range (10^0 – 10^1 W m^{-2}). In general, if the breaking wave-induced turbulence does not penetrate deeply enough into the water column it may not be fully detected by the ADCP because the Doppler signal is affected by the presence of the surface [Thomson, 2012]. The depth to which a breaking wave penetrates the water column depends on the type of breaker [Thornton and Guza, 1983], and most breakers at the FRF were spilling breakers whose dissipation was likely concentrated near the surface. Both laboratory and field in situ estimates of energy dissipation in the surf zone suggest that the majority of wave energy dissipation occurs near the surface, above trough level [Govender et al., 2004; Feddersen, 2012]. Therefore, the in situ TKE dissipation rate estimate from the moored ADCP has the potential to be biased low as a measure of ϵ_{brk} .

The dynamic range of ϵ_{moored} decreases further during the storm, when breaking rate increases due to high winds and large swell. During low tides of this storm, the maximum ϵ_{D81} values increase, as expected, but the maximum ϵ_{moored} values decrease. This unexpected decrease in ϵ_{moored} during the storm is likely due to increased bubble and sediment interference with the ADCP measurements. During high tides of this storm, the breaking rate increases just enough to raise ϵ_{moored} above its noise floor. The D81 estimate is also elevated throughout high tides on 12–13 September 2010, with the wave dissipation rate rarely falling below 1 W m^{-2} .

Outside of storm conditions, high tide values of ϵ_{D81} are in the range of 10^{-2} – 10^{-1} W m^{-2} and can be explained by the near-zero breaking rates at $x = 190 \text{ m}$ during high tide. The D81 model is still physically applicable at low breaking rates, and ϵ_{D81} demonstrates a coherent signal even though these estimates are based on very few events. Although high tide values of ϵ_{moored} are limited by the noise floor and therefore are not comparable to the remotely sensed observations, low ϵ_{D81} values are corroborated by TKE dissipation rate estimates made from SWIFT drifters deployed during the SZO experiment. The ϵ_{SWIFT} noise floor is on the order of 10^{-1} W m^{-2} [Thomson, 2012], lower than that of the moored ADCP. The SWIFT TKE dissipation rate estimates are sparse and represent an average taken over 5 min bursts in time and space, but ϵ_{SWIFT} still provides support for the low wave dissipation rate estimates of ϵ_{D81} during high tide. SWIFT TKE dissipation rates are compared to ϵ_{D81} in Figure 12a for times when the drifter was positioned within the surf zone and near the cross-shore transect ($x = 100$ – 200 m , $y = 600$ – 800 m). For these times (high tide on 11 September 2010 and 13 September 2010), ϵ_{SWIFT} is within an order of magnitude ϵ_{D81} , which constitutes relatively good agreement for turbulent dissipation rates in the surf zone [Feddersen, 2012; Bryan et al., 2003].

3.4. Comparison of Wave Dissipation Models

The D81 dissipation model is easily calculated based on remote sensing data and could be included in near-shore wave and circulation models, so here it is compared against an existing wave dissipation model by *Janssen and Battjes* [2007] to gain a sense of its relative performance. The JB07 wave energy dissipation model is commonly used within nearshore wave and circulation models, such as SWAN [*Booij et al.*, 1999; *Ris et al.*, 1999]. It requires mean wave frequency \bar{f} , the fraction of breaking waves Q_b , root-mean-squared wave height H_{rms} , and depth h ,

$$\epsilon_{JB07} = \frac{3\sqrt{16}}{\pi} B \rho g \frac{H_{rms}^3}{h} \bar{f} Q_b, \tag{34}$$

where B is a parameter with a value near one, ρ is the density of sea water, and g is the acceleration due to gravity [*Janssen and Battjes*, 2007]. The product of \bar{f} and Q_b is the breaking rate, which is equivalent to the ratio of the number of breaking waves in a given sampling period, N_b , to the length of that time period, t_{total} ,

$$\bar{f} Q_b = \bar{T} \cdot \frac{N_b}{N_{total}} \equiv \frac{N_b}{t_{total}}, \tag{35}$$

where \bar{T} is the average wave period and N_{total} is the total number of waves observed during the sample record.

Using (34) and (35), ϵ_{JB07} was estimated using IR and in situ data. $N_b(x)$ was computed from the binary masks of identified breaking waves along the chosen transect, and t_{total} was fixed at 1080 s. H_{rms} and h were derived using the pressure measurement from the ADCP. In order to apply the JB07 model along the entire transect, the model would need to be incorporated into a cross-shore wave evolution model. Therefore, the present analysis was completed at one point in the surf zone ($x = 190$ m).

The D81 and JB07 wave dissipation rate estimates agree well in magnitude and temporal variability on tidal time scales (Figure 12a). The agreement between these two independent estimates is further illustrated by the comparison in Figure 13. The lowest values of ϵ_{D81} and ϵ_{JB07} occur at times when the breaking rate is near zero ($< 0.001 \text{ s}^{-1}$), and the greatest differences between ϵ_{D81} and ϵ_{JB07} occur during the storm. The estimates exhibit a near one-to-one relationship, with an offset that indicates a systematically higher wave dissipation rate predicted by ϵ_{JB07} . A linear fit to ϵ_{JB07} and ϵ_{D81} has a slope of 0.53, with an r^2 value of 0.49, and a root-mean-squared difference of 8.85 W m^{-2} . A linear fit to the log of the estimates yields a slope of 1.13,

an r^2 value of 0.76, and a root-mean-squared difference of 9.04 W m^{-2} . These fits suggest that the low D81 dissipation rates estimated during periods of low breaking rate are meaningful.

While neither D81 nor JB07 is estimated without supplemental in situ measurements in this study, it may be possible to achieve good estimates of wave energy dissipation using D81 with inputs derived only from remote sensing data. JB07, on the other hand, is a function of breaking rate, H_{rms} , and water depth. Breaking rate is remotely estimated, and while H_{rms} is typically measured by in situ wave gauges, it might also be estimated from stereo optical systems [*Benetazzo*, 2006; *Benetazzo et al.*, 2012]. Water depth requires a bathymetric survey or a depth-inversion model [*Holman et al.*, 2013], which may be unavailable. Therefore, the D81 dissipation estimate is a viable alternative parameterization based on remotely sensed data only.

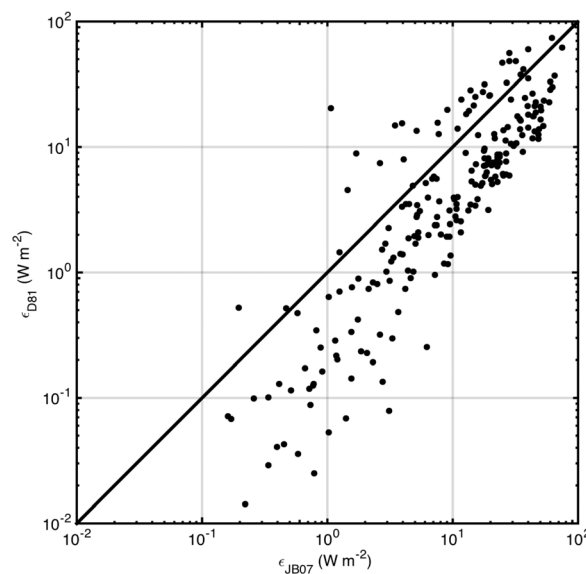


Figure 13. Comparison of ϵ_{D81} and ϵ_{JB07} . A one-to-one line is plotted for reference.

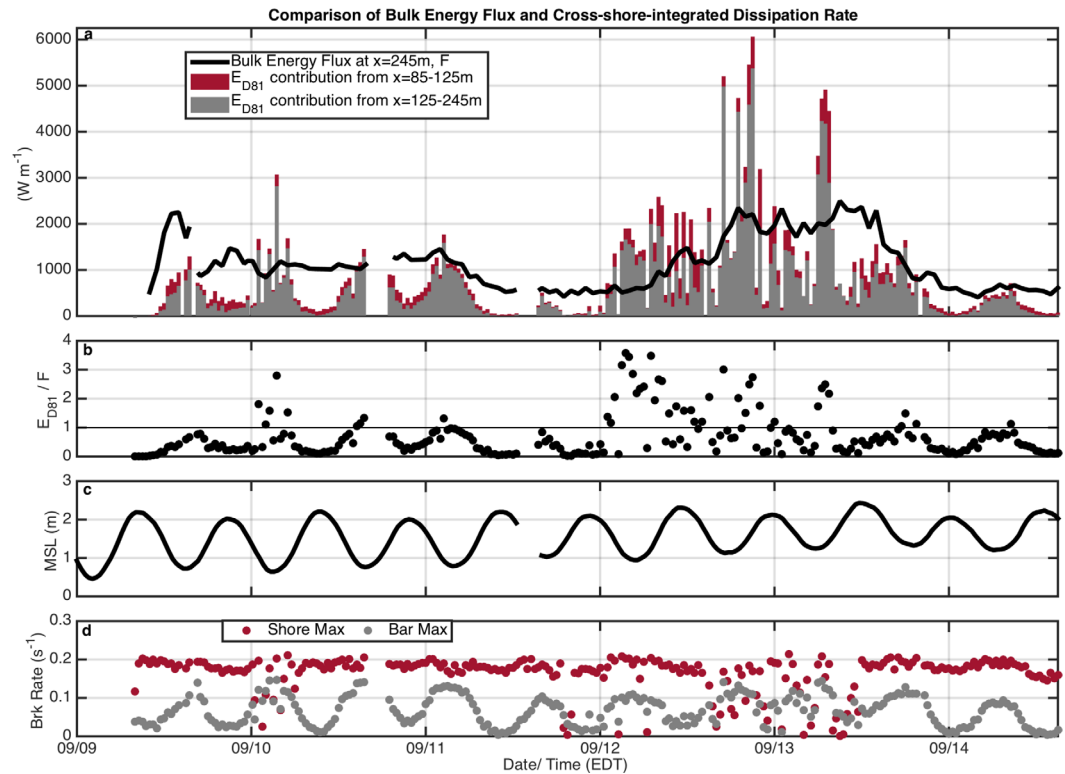


Figure 14. (a) Time series of cross-shore-integrated remote wave dissipation rate estimate E_{D81} (stacked bar graph) and bulk energy flux \mathcal{F} through $x = 245$ m (black curve). E_{D81} is decomposed by cross-shore region: the contribution from shoreward of the bar, $x = 85$ – 125 m (red) and the contribution from the bar to the offshore extent of transect, $x = 125$ – 245 m (gray). (b) Time series of the ratio of E_{D81} to \mathcal{F} . E_{D81}/\mathcal{F} equal to one marked by black line. (c) Mean sea level time series from moored ADCP at $x = 190$ m. (d) Breaking rate time series at the shoreline (red) and near the bar (gray).

3.5. Bulk Energy Flux Estimates

As a further comparison to in situ data, ϵ_{D81} is discretely integrated in the cross-shore direction,

$$E_{D81} = \sum_{x=\text{shore}}^{x=245\text{m}} \epsilon_{D81}(x) \Delta x, \quad (36)$$

yielding the wave energy dissipation rate per unit crest length over the full transect. Figure 14a shows the total E_{D81} (stacked bar graph), shaded by cross-shore region, compared to the cross-shore bulk wave energy flux, \mathcal{F} , entering the surf zone at the offshore edge of the transect. \mathcal{F} is estimated from the 2-D wave energy density spectrum reported by the FRF 3 m ADCP, located near the offshore edge of the transect, using linear wave theory and discretely integrating over all wave directions and frequencies:

$$\mathcal{F} = \sum_f \sum_\phi E(f, \phi) c_g(f) \cos(\phi) \Delta\phi \Delta f. \quad (37)$$

Estimating E_{D81} and \mathcal{F} according to (36) and (37) does not account for wave spreading or focusing, so \mathcal{F} gives an upper bound for the onshore wave energy flux.

The component of E_{D81} calculated near the shoreline (from $x = 85$ – 125 m) is extremely small in comparison with E_{D81} over the bar (for $x = 125$ – 245 m), even though breaking rate remains high in the region shoreward of the bar throughout all stages of the tide. This suggests that the D81 formulation underestimates wave dissipation for breakers at the shoreline, where the assumption that waves are spilling may not be representative of the plunging and surging waves often seen near the shore. Additionally, the contribution to E_{D81} from $x = 125$ – 245 m is large, even at high tide (low breaking rate), because the bar region exhibits larger L_r than the shore region (shown in Figure 10), and ϵ_{D81} has an L_r^2 dependence. \mathcal{F} does not vary with the tide, rather it fluctuates about a mean of $1.1 \times 10^3 \text{ W m}^{-1}$ due to incoming waves with fairly consistent,

slowly varying H_s throughout the experiment (Figure 2). E_{D81} is strongly modified by the tidal fluctuations in breaking rate over the bar (Figure 14c), but lies mostly within 1 order of magnitude of \mathcal{F} . E_{D81} is less than \mathcal{F} for most of the experimental record, as expected. However, E_{D81} exceeds \mathcal{F} briefly on 10 September 2010 and frequently during the storm. One possible explanation for the larger E_{D81} estimates is that the high-wind storm conditions enhanced wave breaking within the surf zone. These wind-aided breaking sea waves will have higher steepness (f_p and H_s increase during this time, Figures 11c and 11d), which may not be adequately represented in the wave slope estimate (Figure 9). Another potential explanation for $E_{D81} > \mathcal{F}$ is that during periods of high breaking rate, sequential breaking crests may merge in the IR imagery. If two waves of the same size merge ($L_{r,merged} = 2L_r$), then the resulting $\epsilon_{D81,merged}$ would be twice as large as the sum of the wave dissipation rate calculated from the two individual rollers due to the squared dependence on L_r .

The ratio of the integrated D81 estimate to the bulk energy flux yields an estimate of the fraction of total incoming wave energy that is dissipated by wave breaking. E_{D81}/\mathcal{F} varies from near 0 to 3.57, oscillating due to the tidally dependent wave breaking dissipation rate estimate. The mean of E_{D81}/\mathcal{F} is 0.69. If values greater than one are excluded, thus removing nonphysical data for which wave energy dissipation through breaking is greater than the total incoming wave energy, the mean of E_{D81}/\mathcal{F} is 0.40. These results suggest that under the observed wind and wave conditions 40–69% of the incoming wave energy is dissipated via wave breaking. Some of the incoming wave energy may also be reflected from the beach. *Elgar and Herbers* [1994] found that reflection ranged from 3% to 18% and was largest for high tide (steep beach) and low-frequency swell waves. The beach slope at the FRF during SZO 2010 varies from 0.105 at high tide to 0.052 at low tide, consistent with those reported in *Elgar and Herbers* [1994], and the dominant swell-sea wave frequencies were also comparable. Therefore, it is reasonable to assume that similar wave reflection occurs during the present experiment, which could account for some of the incoming wave energy not dissipated through wave breaking, especially during high tides. Some of the remaining energy is likely transferred to infragravity waves and currents, further closing the energy balance. However, other method-related causes might produce low bias of remotely sensed dissipation, including underreporting of breaking waves, violation of the spilling breaker assumption in D81, and variation of parameters across the surf zone (i.e., wave slope, roller area similarity, and ρ'). For example, ρ' was defined according to *Duncan* [1981], and because ρ' has not yet been measured in the surf zone, an arbitrary increase or decrease of its value would produce no change in the skill of the estimates.

4. Conclusions

By exploiting the unique signatures of active and residual foam in thermal IR imagery, an algorithm was developed to identify breaking waves in the surf zone. The roller length of each wave was extracted, corrected for image projection, and used to estimate energy dissipation due to wave breaking via the *Duncan* [1981] parameterization. The D81 wave dissipation rate estimates are well correlated with in situ estimates of TKE dissipation. Also, the D81 cross-shore-integrated wave dissipation rate accounted for 40–69% of the incoming bulk wave energy flux estimate computed at the offshore edge of the transect. Both comparisons support the applicability of the D81 parameterization to estimate wave breaking energy dissipation rates in the field. Good agreement was found between the independent D81 and JB07 dissipation rate estimates. Since the JB07 model is often nested within nearshore circulation models, the agreement of the results from D81 and JB07 suggests that the D81 formulation may also work well within nearshore models.

4.1. Future Considerations

Although the spatial distribution of roller length was not explored here, the details of breaking wave evolution revealed in this analysis demonstrate further potential for IR imagery in surf zone studies. The spatial pattern of roller length and the occurrence distribution, evident in Figure 10a, suggests there is a maximum achievable roller length and outlines the conditions for depth-limited breaking at the FRF. This information would be further enhanced by extending the methods for analysis over an area. Two-dimensional maps of roller length would better capture the spatial and temporal variations of energy dissipation due to wave breaking and would be valuable for driving nearshore process models. Processing IR images in two dimensions would also enable the measurement of wave direction on a wave-by-wave basis. With this information, roller projection error could be corrected with higher accuracy. For future experiments, the IR camera

should be optimally positioned to look along the dominant wave propagation direction so that geometry-based errors can be minimized. To improve IR remote sensing capabilities, two IR cameras, one up-looking and one down-looking, could be deployed. The up-looking camera should image the region of sky that is reflected off the sea surface and imaged by the down-looking camera, so that the reflected sky conditions (e.g., cloud and sun position and movement) can be removed from the sea surface images and less normalization would be necessary. IR images might also be used to estimate wave slope. For example, a modulation transfer function might be developed using the dependence of emissivity on incidence angle to invert for wave slope. Wave slope measurements could also be attempted with a stereo imaging system [De Vries *et al.*, 2011; Benetazzo *et al.*, 2012]. An IR-derived, wave-by-wave slope estimate could then be used, with roller length, in the D81 formulation to produce a truly remote estimate of energy dissipation due to wave breaking in the surf zone.

Acknowledgments

This research was made possible by DARLA-MURI funding from the Office of Naval Research (award: N000141010932) and additional student funding from the NDIA UWD Academic Fellowship Program 2011–2012. The authors thank the U.S. Army Corps of Engineers Field Research Facility at Duck, NC, for help with data collection and for providing data from permanent moorings. The authors also thank Dan Clark for his technical support. Finally, the authors appreciate the helpful comments of three anonymous reviewers. Contact corresponding author (rjcarini@apl.washington.edu) for access to the data used in this research.

References

- Aarninkhof, S. G., and B. G. Ruessink (2004), Video observations and model predictions of depth-induced wave dissipation, *IEEE Trans. Geosci. Remote Sens.*, *42*(11), 2612–2622.
- Banner, M. L., A. V. Babanin, and I. R. Young (2000), Breaking probability for dominant waves on the sea surface, *J. Phys. Oceanogr.*, *30*(12), 3145–3160.
- Battjes, J. (1972), Set-up due to irregular waves, *Coastal Eng. Proc.*, *1*(13), 1993–2004, doi:10.9753/icce.v13.
- Benetazzo, A. (2006), Measurements of short water waves using stereo matched image sequences, *Coastal Eng.*, *53*(12), 1013–1032.
- Benetazzo, A., F. Fedele, G. Gallego, P.-C. Shih, and A. Yezzi (2012), Offshore stereo measurements of gravity waves, *Coastal Eng.*, *64*, 127–138.
- Birkemeier, W. A., H. Miller, S. Wilhelm, A. DeWall, and C. Gorbics (1985), A user's guide to the coastal engineering research center's (cerc's) field research facility, technical report.
- Booij, N., R. Ris, and L. H. Holthuijsen (1999), A third-generation wave model for coastal regions: 1. Model description and validation, *J. Geophys. Res.*, *104*(C4), 7649–7666.
- Branch, R., C. Chickadel, A. Jessup, and R. Carini (2012), Abstract OS13E-1782, presented at 2012 Fall Meeting, AGU, San Francisco, Calif.
- Branch, R., C. C. Chickadel, and A. T. Jessup (2014), Thermal infrared multipath reflection from breaking waves observed at large incidence angles, *IEEE Trans. Geosci. Remote Sens.*, *52*(1), 249–256.
- Bryan, K. R., K. P. Black, and R. M. Gorman (2003), Spectral estimates of dissipation rate within and near the surf zone, *J. Phys. Oceanogr.*, *33*(5), 979–993.
- Carini, R. J. (2014), Estimating energy dissipation due to wave breaking in the surf zone using infrared imagery, MS thesis, Univ. of Washington, Seattle.
- Catalán, P. A., M. C. Haller, R. A. Holman, and W. J. Plant (2011), Optical and microwave detection of wave breaking in the surf zone, *IEEE Trans. Geosci. Remote Sens.*, *49*(6), 1879–1893.
- Church, J. C., and E. B. Thornton (1993), Effects of breaking wave induced turbulence within a longshore current model, *Coastal Eng.*, *20*(1), 1–28.
- Collins, J. I. (1970), Probabilities of breaking wave characteristics, *Coastal Eng. Proc.*, *1*(12), 399–414.
- Csanady, G. T. (2001), *Air-Sea Interaction: Laws and Mechanisms*, Cambridge Univ. Press.
- Dally, W. R., and C. A. Brown (1995), A modeling investigation of the breaking wave roller with application to cross-shore currents, *J. Geophys. Res.*, *100*(C12), 24,873–24,883.
- De Vries, S., D. Hill, M. De Schipper, and M. Stive (2011), Remote sensing of surf zone waves using stereo imaging, *Coastal Eng.*, *58*(3), 239–250.
- Duncan, J. (1981), An experimental investigation of breaking waves produced by a towed hydrofoil, *Proc. R. Soc. London, Ser. A*, *377*(1770), 331–348.
- Elgar, R. T. G., and T. H. C. Herbers (1994), Reflection of ocean surface gravity waves from a natural beach, *J. Phys. Oceanogr.*, *24*(7), 1503–1511.
- Elgar, S., R. Guza, B. Raubenheimer, T. Herbers, and E. L. Gallagher (1997), Spectral evolution of shoaling and breaking waves on a barred beach, *J. Geophys. Res.*, *102*(C7), 15,797–15,805.
- Feddersen, F. (2012), Scaling surf zone turbulence, *Geophys. Res. Lett.*, *39*, L18613, doi:10.1029/2012GL052970.
- Fogelberg, R. A. (2003), A study of microbreaking modulation by ocean swell using infrared and microwave techniques, MS thesis, Univ. of Washington, Seattle.
- Gerbi, G. P., J. H. Trowbridge, E. A. Terray, A. J. Plueddemann, and T. Kukulka (2009), Observations of turbulence in the ocean surface boundary layer: Energetics and transport, *J. Phys. Oceanogr.*, *39*(5), 1077–1096.
- Govender, K., G. Mocke, and M. Alport (2004), Dissipation of isotropic turbulence and length-scale measurements through the wave roller in laboratory spilling waves, *J. Geophys. Res.*, *109*, C08018, doi:10.1029/2003JC002233.
- Grasso, F., B. Castelle, and B. Ruessink (2012), Turbulence dissipation under breaking waves and bores in a natural surf zone, *Cont. Shelf Res.*, *43*, 133–141.
- Haller, M. C., and P. A. Catalan (2009), Remote sensing of wave roller lengths in the laboratory, *J. Geophys. Res.*, *114*, C07022, doi:10.1029/2008JC005185.
- Holman, R., N. Plant, and T. Holland (2013), cbathy: A robust algorithm for estimating nearshore bathymetry, *J. Geophys. Res. Oceans*, *118*, 2595–2609, doi:10.1002/jgrc.20199.
- Holman, R. A., A. Sallenger, T. C. Lippmann, and J. W. Haines (1993), The application of video image processing to the study of nearshore processes, *Oceanography*, *6*(3), 78–85.
- Janssen, T., and J. Battjes (2007), A note on wave energy dissipation over steep beaches, *Coastal Eng.*, *54*(9), 711–716, doi:10.1016/j.coastaleng.2007.05.006.
- Jessup, A., C. Zappa, M. Loewen, and V. Hesany (1997a), Infrared remote sensing of breaking waves, *Nature*, *385*(6611), 52–55.

- Jessup, A., C. Zappa, and H. Yeh (1997b), Defining and quantifying microscale wave breaking with infrared imagery, *J. Geophys. Res.*, **102**(C10), 23,145–23,153.
- Kuo, C. T., and S.-J. Kuo (1974), The effect of wave breaking on the statistical distribution of wave heights, in *Civil Engineering in the Oceans III*, pp. 1211–1231, ASCE.
- Lamarre, E., and W. Melville (1991), Air entrainment and dissipation in breaking waves, *Nature*, **351**(6326), 469–472.
- Lanckriet, T., and J. A. Puleo (2013), Near-bed turbulence dissipation measurements in the inner surf and swash zone, *J. Geophys. Res. Oceans*, **118**, 6634–6647, doi:10.1002/2013JC009251.
- Lippmann, T., A. Brookins, and E. Thornton (1996), Wave energy transformation on natural profiles, *Coastal Eng.*, **27**(1), 1–20.
- Madsen, P. A., O. Sørensen, and H. Schäffer (1997), Surf zone dynamics simulated by a Boussinesq type model. Part I. Model description and cross-shore motion of regular waves, *Coastal Eng.*, **32**(4), 255–287.
- Marmorino, G. O., and G. B. Smith (2005), Bright and dark ocean whitecaps observed in the infrared, *Geophys. Res. Lett.*, **32**, L11604, doi:10.1029/2005GL023176.
- Masuda, K. (2006), Infrared sea surface emissivity including multiple reflection effect for isotropic Gaussian slope distribution model, *Remote Sens. Environ.*, **103**(4), 488–496, doi:10.1016/j.rse.2006.04.011.
- Masuda, K., T. Takashima, and Y. Takayama (1988), Emissivity of pure and sea waters for the model sea-surface in the infrared window regions, *Remote Sens. Environ.*, **24**(2), 313–329.
- Niclos, R., V. Caselles, E. Valor, and C. Coll (2007), Foam effect on the sea surface emissivity in the 8–14 μm region, *J. Geophys. Res.*, **112**, C12020, doi:10.1029/2007JC4521.
- Plant, N., R. Holman, M. Freilich, and W. Birkemeier (1999), A simple model for interannual sandbar behavior, *J. Geophys. Res.*, **104**(C7), 15,755–15,776, doi:10.1029/1999JC900112.
- Reniers, A., and J. Battjes (1997), A laboratory study of longshore currents over barred and non-barred beaches, *Coastal Eng.*, **30**(1), 1–21.
- Reniers, A. J., J. Roelvink, and E. Thornton (2004), Morphodynamic modeling of an embayed beach under wave group forcing, *J. Geo. Res. Oceans*, **109**(C1).
- Ris, R., L. Holthuijsen, and N. Booij (1999), A third-generation wave model for coastal regions: 2. Verification, *J. Geophys. Res.*, **104**(C4), 7667–7681.
- Romero, L., W. K. Melville, and J. M. Kleiss (2012), Spectral energy dissipation due to surface wave breaking, *J. Phys. Oceanogr.*, **42**(9), 1421–1444.
- Ruessink, B., J. Miles, F. Feddersen, R. Guza, and S. Elgar (2001), Modeling the alongshore current on barred beaches, *J. Geophys. Res.*, **106**(C10), 22,451–22,463.
- Stive, M. J., and H. J. De Vriend (1994), Shear stresses and mean flow in shoaling and breaking waves, in ICCE 1994: Proceedings of the 24th International Conference on Coastal Engineering, Kobe, Japan; Authors version, ASCE, N. Y.
- Svendsen, I. A. (1984a), Wave heights and set-up in a surf zone, *Coastal Eng.*, **8**(4), 303–329.
- Svendsen, I. A. (1984b), Mass flux and undertow in a surf zone, *Coastal Eng.*, **8**(4), 347–365.
- Thomson, J. (2012), Wave breaking dissipation observed with “swift” drifters, *J. Atmos. Oceanic Technol.*, **29**(12), 1866–1882.
- Thomson, J., B. Polagye, M. Richmond, and V. Durgesh (2010), Quantifying turbulence for tidal power applications, in *OCEANS 2010*, pp. 1–8, IEEE.
- Thornton, E., and R. Guza (1983), Transformation of wave height distribution, *J. Geophys. Res.*, **88**(C10), 5925–5938, doi:10.1029/JC088iC10p05925.
- Thornton, E. B., and R. T. Guza (1986), Surf zone longshore currents and random waves: Field data and models, *J. Phys. Oceanogr.*, **16**(7), 1165–1178.
- Trowbridge, J., and S. Elgar (2001), Turbulence measurements in the surf zone, *J. Phys. Oceanogr.*, **31**(8), 2403–2417.
- Warner, J. C., C. R. Sherwood, R. P. Signell, C. K. Harries, and H. G. Arango (2008), Development of a three-dimensional, regional, coupled wave, current, and sediment-transport model, *Computers and Geosciences*, **34**(10), 1284–1306.
- Wiles, P. J., T. P. Rippeth, J. H. Simpson, and P. J. Hendricks (2006), A novel technique for measuring the rate of turbulent dissipation in the marine environment, *Geophys. Res. Lett.*, **33**, L21608, doi:10.1029/2006GL027050.